Understanding Laser Powder Bed Fusion Surface Roughness

Jacob C. Snyder
Mem. ASME
Department of Mechanical Engineering,
Pennsylvania State University,
3127 Research Drive,
State College, PA 16801
e-mail: jacob.snyder@psu.edu

Karen A. Thole
Mem. ASME
Department of Mechanical Engineering,
Pennsylvania State University,
136 Reber Building,
University Park, PA 16802
e-mail: kthole@engr.psu.edu

Surface roughness is a well-known consequence of additive manufacturing methods, particularly powder bed fusion processes. To properly design parts for additive manufacturing, a comprehensive understanding of the inherent roughness is necessary. While many researchers have measured different surface roughness resultant from a variety of parameters in the laser powder bed fusion process, few have succeeded in determining causal relationships due to the large number of variables at play. To assist the community in understanding the roughness in laser powder bed fusion processes, this study explored several studies from the literature to identify common trends and discrepancies amongst roughness data. Then, an experimental study was carried out to explore the influence of certain process parameters on surface roughness. Through these comparisons, certain local and global roughness trends have been identified and discussed, as well as a new framework for considering the effect of process parameters on surface roughness. [DOI: 10.1115/1.4046504]

Keywords: additive manufacturing, design for manufacturing, laser processes

Introduction

Surface roughness is a major consequence of using many forms of additive manufacturing (AM). Since the emergence of additive manufacturing, many researchers have studied the roughness inherent with the process. In the early days of plastic additive manufacturing, roughness due to the layerwise nature of the process was the primary focus. However, with the advent of metal-based additive manufacturing, the layerwise roughness is only one of the many different types of roughness that can be generated in this process. With the recent push to use metal additive manufacturing for advanced designs in a production capacity, fully understanding the surface roughness mechanisms in these processes is paramount.

The focus of this study is on understanding the roughness generated by the laser powder bed fusion (L-PBF) process. In this process, metal powders are melted using a tightly focused laser to form each layer of a part. Because of its ability to create fine details using a variety of metal alloys, L-PBF is currently one of the most commonly used forms of metal additive manufacturing across a variety of industries. However, this process involves a number of highly complex physical phenomena that contribute to roughness generation. This paper approaches understanding L-PBF roughness by first examining the literature surrounding additive surface roughness, as well as providing background on the types of surface roughness and scaling methods common with L-PBF. Following the background, results from an abbreviated experimental study are presented to highlight different roughness phenomena and illustrate important factors to consider when attempting to control the roughness of L-PBF parts.

Review of the Literature

Surface roughness has long been a metric of interest in L-PBF additive manufacturing research. Since process development testing typically involves fabricating many small cubes, many studies in the literature have evaluated the roughness on the top surface of these cubes [1–21]. Of the studies that provide sufficient process parameter information, most see a common trend whereby the roughness scales with energy density input to the surface. Studies by Spierings et al. [8], Yang et al. [22], Casalino et al. [13], and Liu et al. [19] all saw the same basic trend as shown by Wang et al. [9] in Fig. 1. In the first section of the trend, the mean roughness magnitude (R_a) decreases with energy density. This behavior is typically attributed improved melting of the surface. The porosity ($1-\rho/\rho_{solid}$) data shown in Fig. 1 support this explanation, whereby the material is becoming less porous as the energy density is increased. The roughness decreases with energy density to some optimal value, before switching directions and increasing with energy density. This increase in roughness at higher energy densities is attributed to material vaporization, which is also supported by the increase in porosity.

Despite the fact that this roughness trend is common in the literature, several studies have shown that energy density does not scale upskin (US) surface roughness results well [2,5,23]. In particular, these three studies evaluated geometries other than small cubes or used laser powers and speeds higher than those utilized by other researchers, hinting at the fact that volume energy density may not be the best scaling for all process regimes or more realistic part geometries.

Fewer studies in the literature have explicitly looked at the roughness of the downskin (DS) surfaces. It is relatively well known that these surfaces exhibit the highest roughness in L-PBF since material is being built upon powder instead of solid material, but only a few studies have examined them [23–29]. Most of these studies show higher roughness magnitudes than the upskin surfaces (20 to 65+ μm), which does not scale well with the process parameters. Many attribute the high levels of roughness to the decreased

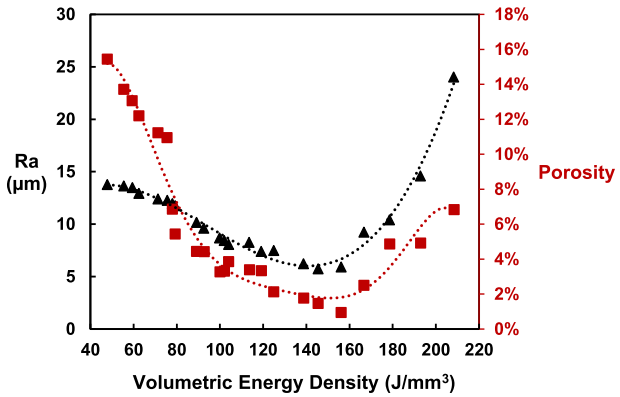

Fig. 1 Upskin mean roughness magnitude (black triangles) and porosity of the part (red squares) versus volumetric energy density, recreated from Ref. [9] (Color version online.)

Manuscript received April 3, 2019; final manuscript received February 13, 2020; published online February 28, 2020. Assoc. Editor: Sam Anand.

thermal conductivity of the powder underneath the melt pool. For example, the study by Tian et al. [23] used simple melt depth predictions with powder properties to show that downskin roughness was minimized when the melt depth was similar in size to the layer thickness.

A few early studies evaluated the ability to use a laser to remelt rough surfaces to decrease the roughness magnitude [17,30–34]. This method proved to be very effective at reducing roughness, with reductions of 90% in certain cases [30]. Laser remelting has found its way into current L-PBF by way of contour scanning, whereby a single laser pass at the edge of a layer follows the hatching to reduce the surface roughness (contours may also be defined prior to the hatching, but there is little available in the public literature showing the benefits of pre- versus post-contours). There have been relatively few studies to examine the roughness of contours themselves [22,23,26,29,35]. The general consensus is that contours do reduce the roughness magnitude, but scaling the results has proved inconclusive. For example, contour parameter changes by Fox et al. [26] failed to generate significant differences in roughness, while contour parameter changes by Koutiri et al. [29] produced two opposing roughness trends for downskin surfaces. Therefore, the effects of contours on roughness are still a relatively unexplored area.

Some studies have also shown that the hatching pattern itself plays a role in the development of the surface roughness [16,24,25,36,37]. For example, Kudzal et al. [37] evaluated a number of common hatching patterns and showed the resultant differences in morphology and roughness magnitude of the surfaces. Another study by Depond et al. [16] used *in situ* roughness measurements of the top surface to show that non-rotating scan vectors resulted in a layerwise accumulation of roughness. However, there has been little work in the public literature on the presence of patterns in surface roughness of more realistic part geometries.

Another subset of studies has investigated the role of the powder on surface roughness [1,8,38]. While the powder seems like a natural driver of surface roughness given the presence of partially melted particles on many L-PBF surfaces, results show that the powder size does not have a strong influence on roughness. In a study by Liu et al. [38], powder with a smaller mean particle size was shown to result in a 10–30% lower roughness for vertical surfaces using a given set of laser parameters. However, when considering the top surface, no significant difference was measured among the different powder sizes. Similarly, some studies have investigated the role of powder reuse on surface roughness. While reuse cycles can impact the shape and chemistry of metal powders, a study by Del Re et al. [39] showed no significant effect on surface roughness. Ultimately, differences in powder characteristics are too subtle to have a strong impact on surface roughness dominated by laser parameter effects. However, the powder feedstock parameters are nonetheless important to control in the AM process.

Overall, the topic of L-PBF surface roughness has been covered in a wide breadth of studies, but proposed scaling and correlations have been largely anecdotal. Roughness generation in powder bed fusion is a complex process, with many different physical phenomena contributing at a wide range of length and time scales. This study seeks to explore some of these phenomena in a more general sense in an attempt to build a fundamental understanding of the mechanisms of roughness generation in laser powder bed fusion.

Types of Surface Roughness

The roughness generated in the L-PBF process can take many forms. These different forms of roughness have varying length scales, shapes, and physical mechanisms driving their creation. Thus, it is important to understand differences among them. The type of roughness that many associate with powder-based AM methods is the presence of partially melted particles [26,40–42]. Examples of surfaces with partially melted particles are shown in Fig. 2. For some surfaces, partially melted particles are simply a result of having extremely hot surfaces in contact with unmelted powder. As the area surrounding a laser pass cools, the neighboring powder melts or sinters to the hot surface. This behavior is particularly true for downskin surfaces; however, upskin surfaces also feature partially melted particles despite a lack of surrounding powder. As shown by Matthews et al. [42] and Bidare et al. [43], the complex fluid flow caused by the laser material interaction and the inert gas flow above the powder bed can entrain powder, depositing it onto otherwise smooth upskin surfaces. Laser material interactions as well as inert gas flow and scanning strategy can all influence the upskin partially melted particles. Previous studies examining fluid mechanics with AM parts have hypothesized that the dominant roughness length scale is the powder particle size [41]. However, as will be discussed herein, the particle size is simply one of many roughness length scales present, with its significance controlled by the process parameters employed for a particular surface.

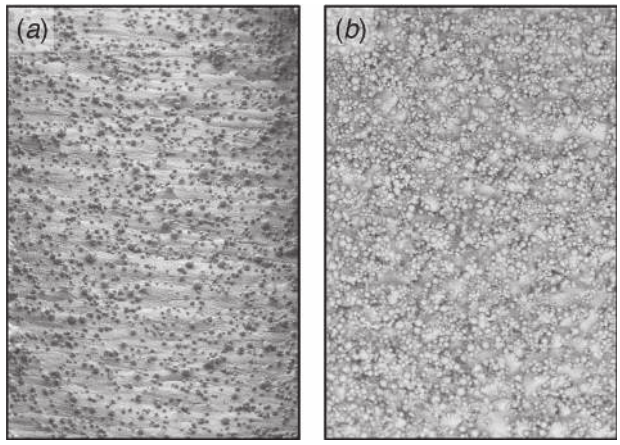

Fig. 2 Partially melted powder particles on (*a*) upskin and (*b*) downskin surfaces. Width of images is 1.8 mm.

Moving up in length scale, the next type of L-PBF roughness can be attributed to the hatch spacing. Without an optimal hatch spacing, subsequent laser passes can form large ridges between passes. An extreme example of this phenomenon from a study by Yadroitsev and Smurov [12] is shown in Fig. 3. The roughness due to hatch spacing is most pronounced on upskin surfaces but also has an effect on side surfaces. For example, Tian et al. [23] have developed a simple geometric relationship which scales the roughness on these side (vertical) surfaces with the hatch spacing.

Another type of roughness commonly referenced in the L-PBF literature is balling. There is some variation in what is referred to as balling in the literature, but typically balling refers to features that form as a result of the molten material attempting to minimize its surface energy by breaking up into smaller spheres. This behavior is an example of a Plateau-Rayleigh instability most commonly seen when the melt pool is thin and elongated. However, there are other intra-meltpool physics such as Marangoni convection, which also affect the melt pool stability [44]. Instead of fully breaking into small spheres, an elongated meltpool can also begin to neck, resulting in a sinusoidal wavy cross section. This phenomenon is sometimes referred to as humping.

If sufficient energy is not provided to fully melt the powder feedstock, the resultant surface can exhibit another type of roughness known as lack of fusion. This type of roughness is typically measured on upskin surfaces and correlates with porosity/relative density as shown in Fig. 1 from the study by Wang et al. [9]. The roughness data at the low energy densities, regions A and B, were attributed to lack of fusion roughness.

The last and potentially largest scale of roughness is dross. Dross can be loosely defined as excess material created by improper

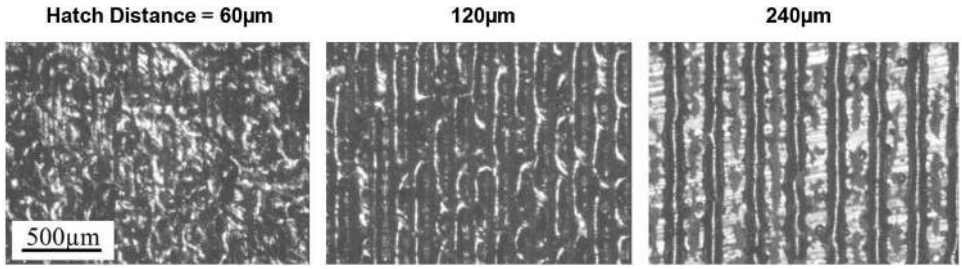

Fig. 3 Surfaces with three different hatch spacings, taken from Ref. [12] (Reprinted with permission from Elsevier © 2011)

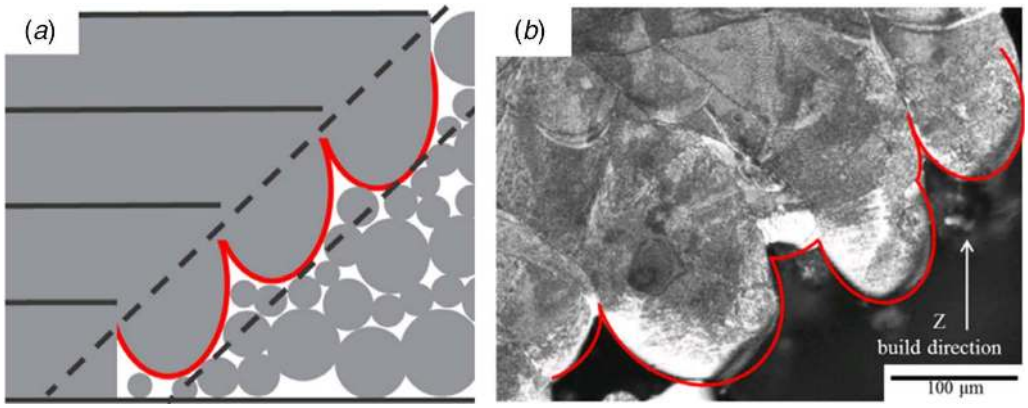

Fig. 4 Figure from Ref. [23] (Reprinted with permission from Elsevier © 2017) showing dross on a 45 deg downskin surface in (*a*) schematic and (*b*) micrograph cross section

control of the meltpool while welding. Typically dross is seen when creating overhangs or downskin surfaces. Despite the vast number of studies looking at L-PBF surface roughness, few actually address downskins and this source of roughness, which is one of the main challenges to resolve for parameter development. For these downskin surfaces, building over powder results in large variations in thermal properties, making control of the melt pool much more difficult. Typically, dross is formed on downskins as a result of too much energy input to these regions. This excess energy causes the meltpool to penetrate far deeper than intended, as shown by Tian et al. [23] and given in Fig. 4. While many think of layer thickness or powder particles as the dominant length scales of AM roughness, the fact is that dross features can be many times larger than these scales. Much of the roughness on downskin surfaces is a result of dross.

Scaling the L-PBF Additive Process

Determining an appropriate scaling for additive manufacturing processes has proven somewhat elusive for researchers in this area. A common approach is to start with the amount of energy input by the laser, while accounting for other parameters such as the scan speed (v), hatch spacing (H_d), layer thickness (t), and laser spot size (a). One simple metric that can be calculated is the linear energy density, defined as the laser power divided by scan speed. This metric, shown in Eq. (1), has been used by some authors to successfully optimize parameters for single scan tracks [45,46]. The linear energy density (E') is a logical choice for single laser passes but leaves out many other important variables in the process.

$$E' = \frac{P}{v} \tag{1}$$

To better scale the energy input to the weld, some authors consider the surface energy input by introducing another length scale. One approach is to incorporate the diameter of the laser spot, since the area over which the laser energy is added defines the intensity of the energy. Some studies [13,19,29] have used this definition of surface energy density (E'') to scale roughness results with limited success. Another surface energy input definition that is common in the literature takes into account the hatch spacing (H_d) instead of the laser spot size (a). Conceptually, this definition makes sense when considering that 2D layers are created by consecutive laser passes which need to be appropriately spaced. These two definitions of surface energy density are shown as follows:

$$E'' = \frac{P}{va} \quad \text{or} \quad E'' = \frac{P}{vH_d} \tag{2}$$

The most common parameter in the literature used to scale additive results is the volumetric energy density (E'''), shown in Eq. (3). This parameter divides either of the previous definitions of the surface energy flux by the layer thickness (t). The layer thickness is important to take into account since thicker layers require more energy to be adequately melted.

$$E''' = \frac{P}{vH_d t} \tag{3}$$

While these scaling parameters have been shown to successfully scale roughness magnitude in certain studies [8,9,13,23,38], other work has shown that the roughness does not scale well with these parameters [2,5,23]. Moreover, these scalings do not translate well between materials. The issue is that these scalings are based on energy input only and do not account for the response of the material. The melt pool generated by a given amount of energy input will differ depending on the absorptivity and thermal diffusivity of the material, as well as the boundary conditions of the melt pool, which are determined by the geometry of the part being fabricated. These thermal properties can also vary based on the parameters of the powders used as a feedstock. Thus, a more universal scaling method should account for the response of the material.

Bertoli et al. [47] have recognized the shortcomings in using the energy density to scale additive results. Their work showed that even at matched energy density, the melt pool could vary significantly in shape and size depending on the values of power and speed. In searching for a scaling to predict keyhole formation and weld track shape, Bertoli et al. used the model proposed by King et al. [48] and Hann et al. [49] which related the melt pool depth to the ratio of energy deposited over the enthalpy of melting. This scaling worked to collapse their experimental data on melt pool depth.

The success of this scaling was further explored by Rubenchik et al. [50] to develop relationships for melt pool depth, width, and length as a function of two non-dimensional parameters. The first parameter, β, relates the energy input by the laser to enthalpy of melting for the material. The laser input energy accounts for the laser power (P), laser spot radius (a), and laser scan speed (v), as well the absorptivity (A) and thermal diffusivity (α) of the material. For successful melting, β must be greater than unity. The second non-dimensional parameter, p, relates the thermal diffusion time scale (t_α) to the time necessary for the laser to traverse its own diameter (t_{dwell}).

$$\beta = \frac{\Delta H}{h_s} = \frac{AP/\sqrt{\pi\alpha v a^3}}{\rho C T_m} \tag{4}$$

$$p = \frac{t_\alpha}{t_{\text{dwell}}} = \frac{\alpha/v^2}{a/v} = \frac{\alpha}{av} \tag{5}$$

Rubenchik et al. [50] used numerical methods to determine the response of melt pool geometry to these non-dimensional parameters. This solution was then approximated by three different algebraic expressions to allow the quick calculation of melt pool depth, width, and length based on β and p. The forms of these expressions are shown visually in Fig. 5 over their valid ranges of β and p. From these plots, the difference in sensitivity of melt pool geometry to β and p is evident. For example, at low p values, the melt pool length is predicted to be a much stronger function of β than depth or length. Therefore, using the expressions shown in Fig. 5 to predict the melt pool size will help to provide insight into the roughness results discussed in the following sections.

Experimental Methods

To explore the effect of different process parameters on surface roughness, an experimental study was carried out. Test elements were manufactured with an EOS M280 L-PBF machine in-house, followed by characterization with destructive methods. A combination of used and virgin EOS Hastelloy-X powder with mean particle size of 35 μm was used for the feedstock. A test matrix with 12 different cases was developed to explore certain phenomena, as opposed to using a statistical framework. Many researchers have attempted using statistical frameworks to develop correlations [2,33,51–54], but few have found success due to the plethora of parameters to take into account. In the current study, the parameters varied among the cases were the laser power (P), scanning speed (v), and hatch spacing (H_d) for the upskin and downskin. Laser power and scan speed were also varied for the contours. A full listing of the test cases and parameters used is given in Table 1. These parameter ranges were selected based on a review of the open literature, the L-PBF machine manufacturer's recommendations, and previous experiments by the authors' research group.

The test element geometry used for this study is shown in Fig. 6. The overall design was intended to emulate test coupons supporting a separate study. Consequently, the three rectangular channels that pass through the main portion of the part were the surfaces of interest. A build orientation of 45 deg was chosen to match the coupons in the separate study, with the aim of studying realistic surfaces that are not oriented orthogonally to the build plate. All of the test elements in the current study were arranged near the center of the build plate, with the parameters assigned randomly to minimize position dependence effects.

After the build was complete, the parts were stress relieved under vacuum at 663 °C for 2 h. Wire electro-discharge machining was first used to remove the parts from the plate. Then, each part was sliced down the middle of the outermost internal channel to allow characterization of the upskin and downskin surfaces indicated in Fig. 6.

Roughness characterization was performed using optical profilometry (OP) and scanning electron microscopy (SEM). The OP data provided quantitative measurements of the surface height, while the SEM images provided qualitative information about the surface morphology. It was important to have the SEM images to understand the surfaces given the limitations of OP in resolving overhanging features [55]. The resolution of the optical profilometer was 1.64 μm in the lateral direction and $\ll$1 μm in the normal direction.

The quantitative roughness measurement calculated in this work was the arithmetic mean roughness (S_a). There are many types of roughness metrics that can be used to describe AM roughness [56]; previous work by the current authors has shown that S_a is currently a reasonable metric to scale heat transfer and friction results [55]. Additionally, S_a and its linear corollary R_a are the most commonly reported roughness metrics in the literature. While an entire paper could be devoted to examining the best roughness metric to describe the nuances of AM roughness, the current study was limited to only considering S_a to limit the scope of the discussion.

The arithmetic mean roughness (S_a) was defined as an average of the roughness heights relative to a polynomial surface that was fit to the data to remove any large-scale curvature. This roughness

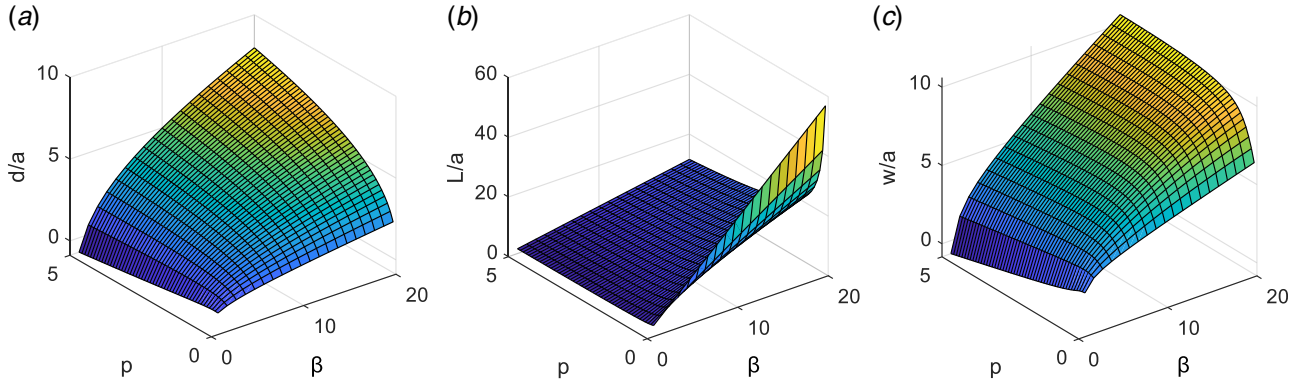

Fig. 5 Variation of non-dimensional melt pool: (*a*) depth, (*b*) length, and (*c*) width based on non-dimensional parameters p and β, using equations proposed by Rubenchik et al. [50]

Table 1 Laser parameters and roughness measurements for all test elements

				Hatching				Contour			
Sample #	Surface	S_a (μm)	±95% (μm)	P (W)	v (mm/s)	H_d (mm)	E'' (J/mm^2)	P (W)	v (mm/s)	Laser BO (mm)	E' (J/mm)
1	US	14.44	4.4	285	960	0.11	2.70				
	DS	38.43	7.6	285	960	0.11	2.70				
2	US	13.29	2.5	110	600	0.09	2.04				
	DS	27.40	2.1	109	2400	0.05	0.91				
3	US	18.62	2.2	76	600	0.09	1.41				
	DS	36.78	3.0	72	2400	0.05	0.60				
4	US	16.26	2.5	255	1000	0.09	2.83				
	DS	26.91	3.5	72	1200	0.05	1.20				
5	US	11.28	2.4	153	600	0.09	2.83				
	DS	26.59	3.6	145	2400	0.05	1.21				
6	US	12.05	2.5	255	1000	0.09	2.83	138	420	0	0.33
	DS	18.54	1.8	72	1200	0.05	1.20	140	1400	0	0.10
7	US	7.18	3.4	153	600	0.09	2.83	138	420	0	0.33
	DS	26.28	4.2	145	2400	0.05	1.21	140	1400	0	0.10
8	US	7.96	3.7	76	600	0.09	1.41	138	420	0	0.33
	DS	19.97	0.9	72	2400	0.05	0.60	140	1400	0	0.10
9	US	8.88	3.0	153	600	0.09	2.83	214	840	0	0.25
	DS	20.91	3.4	145	2400	0.05	1.21	144	2400	0	0.06
10	US	7.67	0.3	153	600	0.09	2.83	107	420	0	0.25
	DS	20.25	1.9	145	2400	0.05	1.21	120	2000	0	0.06
11	US	8.49	1.9	153	600	0.09	2.83	88	700	0	0.13
	DS	25.49	3.3	145	2400	0.05	1.21	72	2400	0	0.03
12	US	16.34	1.5	153	600	0.09	2.83	176	1400	0	0.13
	DS	23.42	1.8	145	2400	0.05	1.21	84	2800	0	0.03

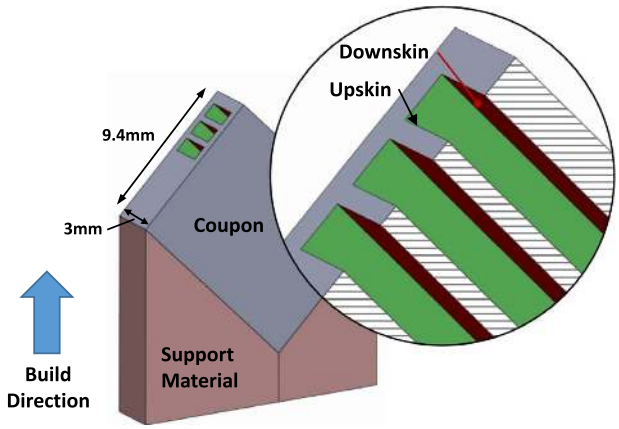

Fig. 6 Test element geometry manufactured to evaluate surface roughness in this study

magnitude was measured at multiple locations on the surfaces of interest to establish a representative average roughness value. These values, along with the 95% confidence interval, are also given in Table 2. Repeatability of these measurements will be discussed in the next section.

Table 2 Melt pool size predictions for upskin based on the Rubenchik model [50]

Sample #	w/H_d	d/t	L/w	S_a (μm)	±95% (μm)	P (W)	v (mm/s)	H_d (mm)	E'' (J/mm^2)
1	2.2	2.1	7.6	14.4	4.4	285	960	0.11	2.7
4	2.5	1.9	7.3	16.3	2.5	255	1000	0.09	2.8
5	2.5	1.9	4.5	11.3	2.4	153	600	0.09	2.8

For a separate analysis, X-ray computed tomography was used on certain coupons to characterize the internal dimensions. Before cutting the samples open, certain samples were scanned using a resolution of 29 μm. With this resolution or voxel size, the computed X-ray tomography (CT) scans only captured the large roughness features of the channels.

Effect of Process Parameters on Roughness

For each particular surface of a test element channel, the effect of a given set of process parameters on roughness was evaluated using optical profilometry and SEM images. Using these methods, the following section considers different parameter effects for the hatching and contours.

Repeatability of Data. Before examining the impact of different parameters on surface roughness, it was first important to establish the variation due to variables that are not controlled within the experiment. Test elements with identical parameter sets were built in multiple locations on the plate to capture the effects of variables such as laser spot variation, inert gas flow effects, and recoater blade interference. Two different rotations of the test elements relative to the plate were also examined, forward (F) and right (R). Lastly, test elements manufactured in two different builds (1 and 2) were compared to establish the repeatability between subsequent builds. The locations of the parts during the main build and repeatability build are shown in Figs. 7(*a*) and 7(*b*), respectively. Parts grayed out in the images of the plate were manufactured for separate studies.

Results comparing the different builds and locations on the plate are shown in Fig. 8(*a*). The "low" build plate position shows the largest deviation in roughness magnitude from the rest of the test cases for the forward angled test element. This result is consistent with that of Kleszczynski et al. [28] where outward angled surfaces near the edge of the build plate were rougher as a result of

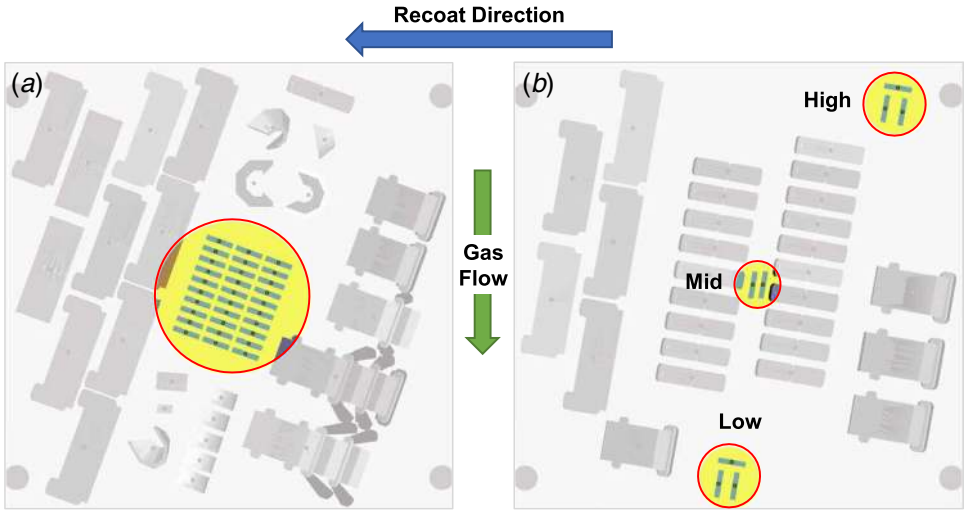

Fig. 7 Locations of test elements on build plate for (*a*) build 1 and (*b*) build 2

deviations from the ideal laser spot shape due to extreme beam angles. Because of this phenomenon, the test elements for the main build were placed near the center of the build plate. Figure 8(*a*) shows the variation in roughness with rotation angle in this mid region to be lower than the low region. Additionally, Fig. 8(*a*) shows good repeatability between the two builds.

Lastly, Fig. 8(*b*) shows the variation of roughness magnitude for both the upskin and downskin surfaces among three identical samples. These samples were built with the same parameters as sample 7 and randomly located within the main build. When considering deviation from an average roughness value, the variation was within 13% for the upskin surfaces and within 1% for the downskin surfaces. These variations are similar to the 95% confidence interval levels for the roughness measurements; therefore, the differences in roughness outside the confidence interval of S_a can be assumed to be significant.

Hatching Effects. The effect of the process parameters on surface roughness was first considered for different cases without any contours. While contours have been shown to improve surface roughness [22,23,26,29,35], the addition of contours can significantly increase the build time. A simple analysis of scanning strategies shows that the build time of parts using contours scales with the surface area to volume ratio of the part. Since many AM parts feature high surface area to volume ratios, it was essential to first consider the surface roughness in cases where no contours are used.

First, three cases are considered where all hatching parameters were matched except for the laser power. The images in Fig. 9 show the upskin (*a*–*c*) and downskin (*d*–*f*) surfaces at three different laser powers. At the bottom of each image, the roughness magnitude and confidence interval are given, as well as the sample number for reference. For the upskin, the laser power was increased linearly from 75 to 153 W. Since all the other parameters remained constant, the increase in power can also be considered as a commensurate increase in E'''. From the images and roughness measurements, the increase in laser power resulted in a decrease in surface roughness, which is consistent with the findings of many studies [8,9,13,19,22] as highlighted in Fig. 1. For upskin surfaces, the high roughness levels at low energy inputs can be attributed to insufficient melting of the powder feedstock.

A similar trend in roughness magnitude is seen with the downskin surfaces shown in Figs. 9(*d*)–9(*f*). The power on the downskin was increased from 72 to 145 W at a constant speed of 2400 mm/s, resulting in a decrease in surface roughness. This result is somewhat surprising given the propensity of roughness on the downskin due to dross from excessive energy input [23]. However, the results here indicate that like the upskin, there is an optimum level of energy density to minimize surface roughness for the downskin. Deviating from this optimum results in an increase in roughness. This hypothesis is supported by looking at the features outlined in red in the images of Fig. 9. Large roughness features caused by the ends of the hatching are visible for both upskin and downskin at the low energy density case, indicating the melt pools were not large enough to create a uniform surface. At the high energy

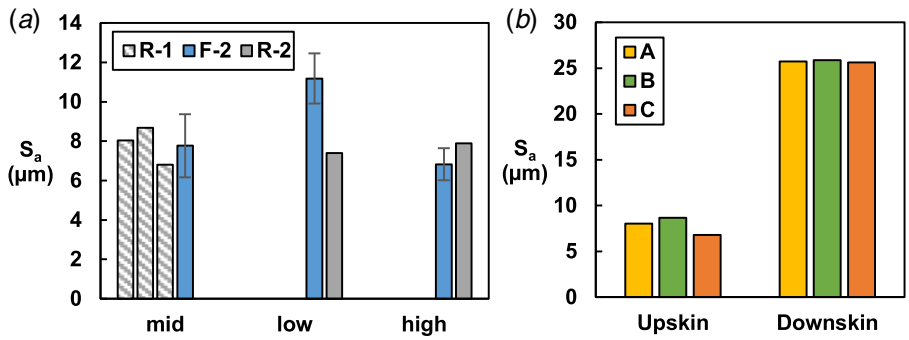

Fig. 8 (*a*) Upskin roughness magnitude compared between builds (1, 2) at three different locations (low, mid, and high) on build plate and two different orientations (F, R). (*b*) Roughness magnitude for upskin and downskin compared for three coupons from the same build with identical parameters.

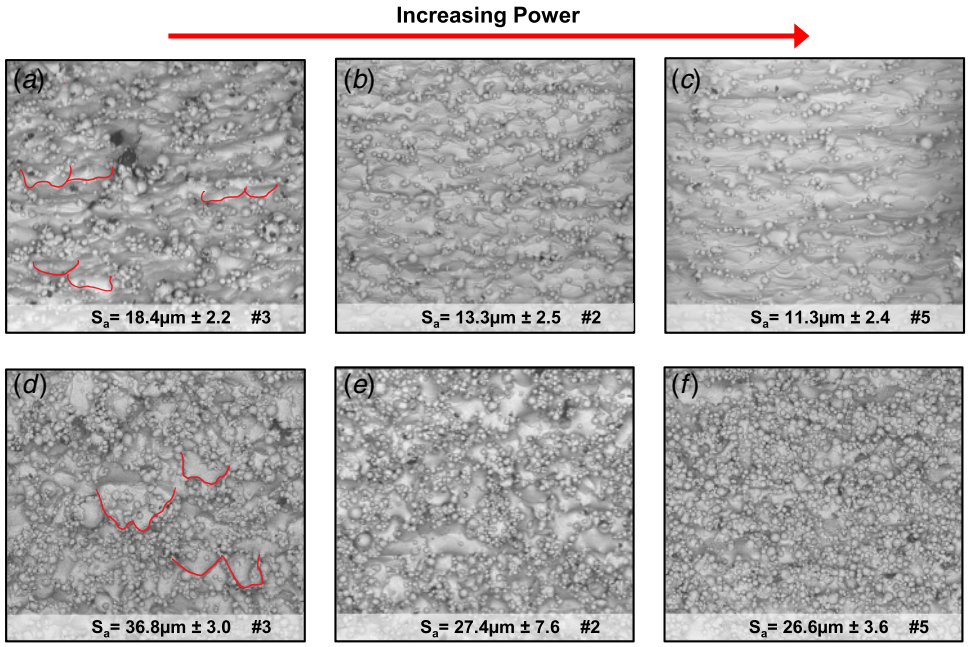

Fig. 9 SEM images showing the effect of laser power on roughness for (*a*)–(*c*) upskin and (*d*)–(*f*) downskin. Red outlines highlight ends of melt pools contributing to surface roughness. Width of images is 1.4 mm. (Color version online.)

density case, however, both the upskin and downskin surfaces appear more uniform (despite the partially melted particles on the downskin).

However, as discussed previously, the energy density does not tell the whole story. If we consider three upskin cases with matched or similar energy densities, but different hatch spacings, laser powers, and scan speeds, the roughness results are not the same, as can be seen in Fig. 10. Both the morphology and magnitude are noticeably different. Sample 1 shows deep pits and cavities, sample 4 shows wide melt pool profiles, while sample 5 shows tightly spaced melt pool profiles. Despite having the same energy density, the difference in roughness magnitude was as large as 44% between the two extreme cases.

To help explain these differences, the melt pool size for these three cases was predicted using the Rubenchik [50] model described previously. Bulk thermal properties of Hast-X at 600 °C, shown in, were used to calculate non-dimensional parameters p and β for the model. A temperature of 600 °C was used as a reference temperature for the thermal properties to capture the elevated thermal conductivity of Hastelloy-X at high temperatures.

Figure 10 shows the values obtained from the melt pool model for samples 1, 4, and 5. Examining the non-dimensional values of aspect ratio (L/w) and relative melt pool width (w/H_d) shows some interesting trends. First, the largest difference between samples 1 and 4 was the 14% increase in the relative melt pool width. This difference can be seen in the morphology in Fig. 10, where the ends of the hatching are more visible in sample 1 than sample 4. With the higher relative melt pool width, there was more overlap between scan vectors, reducing the pits and cavities seen in sample 1. The decrease in depth of the melt pool by 10% may have caused the roughness to increase slightly. However, given the confidence interval of the measurements, samples 1 and 4 effectively have the same roughness magnitude.

Comparing samples 4 and 5 shows that the only change in melt pool dimensions was the 38% reduction in aspect ratio. However, this reduction in aspect ratio of the melt pool resulted in a significant difference in the roughness magnitude. Given the elongation of the melt pool, the change in roughness is attributed to Plateau-Rayleigh instabilities generating irregular melt pool shapes. In addition, large spherical features much larger than the powder can be seen across the surface. These features are suspected to be molten material broken off from the melt pool as it was attempting to minimize its surface energy. Ultimately, these results show that the melt pool physics play a large role in the formation of the roughness and that matching E''' does not necessarily result in the same roughness.

Conversely, on the downskin surfaces, matching the volumetric energy density at different laser powers and speeds resulted in similar roughness magnitudes. Figure 11 shows that these surfaces

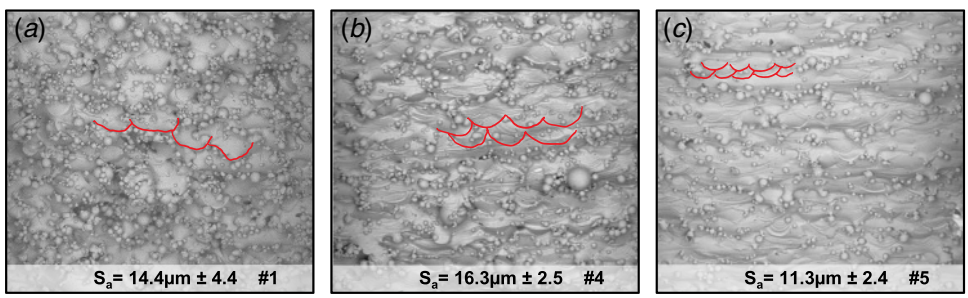

Fig. 10 SEM images of upskin surfaces with matched E''': (*a*) 2.7, (*b*) 2.8, and (c) 2.8, but different scanning speeds, laser powers, and hatch spacing. Red outlines highlight ends of melt pools. Width of images is 1.4 mm. (Color version online.)

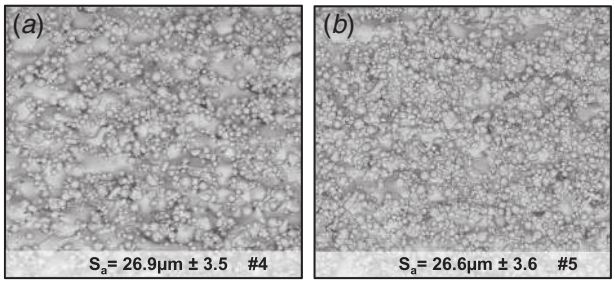

Fig. 11 SEM images of downskin surfaces at matched E''' with different laser powers and scanning speeds. Width of images is 1.4 mm.

appear similar as well. This difference in response of the downskin and upskin surfaces to parameter changes is hypothesized to be a result of different roughness mechanisms. While the roughness on the upskin surface is driven by the length, width, and depth of the melt pool via different phenomena, the roughness of the downskin is most strongly tied to the depth of melt pool alone.

To connect these dimensions to process parameters, the plots in Fig. 5 can be examined to understand the trends of d, L, and w with p and β determined by the Rubenchik [50] model. Recall that p represents the ratio of diffusion to laser dwell times, while β represents the ratio of enthalpy input to enthalpy of melting. For low values of p, the melt depth is a much weaker function of β than the melt length. Therefore, changes in β caused by changes to laser power and scanning speed will have a much greater effect on the melt pool dimension responsible for roughness on the upskin compared to the downskin. This result is interesting, showing that to control roughness, the importance of specific parameters varies depending on whether the surface is an upskin or downskin.

Given the success of the melt pool geometry in explaining the effect of the parameters on roughness, scaling the hatching roughness using the melt pool geometry was attempted. For the upskin, the effect of depth, width, and length was considered together as a non-dimensional volume defined by Eqs. (6) and (7). This parameter attempts to account for roughness due to balling ($\tilde{L}$), hatch spacing ($\tilde{w}$), and lack of fusion ($\tilde{d}$).

$$\tilde{L}=\frac{L}{w},\quad \tilde{w}=\frac{w}{H_d},\quad \tilde{d}=\frac{d}{t} \tag{6}$$

$$\tilde{V}=\tilde{L}\tilde{w}\tilde{d}=\frac{Ld}{H_d t} \tag{7}$$

Figure 12 shows a comparison of scaling the roughness data in this study with volume energy density versus scaling with non-dimensional melt pool volume. Also shown on these plots are roughness data from other studies in the literature that used different materials: 316L [52], AlSi10Mg [2], Hastelloy-X [23], and Ti6Al4V [18,51]. The roughness measurements were made on similar upskin surfaces. Properties used for these different materials were evaluated at a temperature approximately 50% of the melting range for the particular alloy—values are given in Table 3. For some of these cases from the literature, the correlation predicted negative melt pool widths and/or lengths as a result of p values lower than the range covered by the algebraic expression ($p=0.1$–5). These cases with negative dimensions were omitted from the plot, encompassing all of the Hast-X data and much of the Ti6Al4V data.

While there is a bit of scatter in the data shown in Fig. 12(*b*), there is a much clearer trend in roughness using the melt pool volume scaling as opposed to the volumetric energy density scaling shown in Fig. 12(*a*). Note that this trend is similar to that seen by researchers when using an energy density scaling for a single material, as shown in Fig. 1, where there is an optimum roughness condition. Some of the scatter may be explained by other effects in the process not accounted for by melt pool size, such as partially melted particles and position dependence. Additionally, the Rubenchik model is sensitive to the material properties and initial temperature, which may vary considerably among these cases. Nonetheless, using a scaling which takes into account the size of the melt pool shows promise in collapsing roughness data for different materials, machines, and laser spot sizes.

Scaling for the downskin was also attempted, but the same non-dimensional melt pool volume could not be evaluated due to erroneous L and w values caused by the correlation exceeding the valid p range of the model. However, as discussed previously, it is hypothesized that the downskin roughness is most tied to the melt pool depth. Thus, only the depth of the meltpool was calculated for the downskin cases from this study and from literature data [23,57]. For the depth predictions, the bulk conductivity was scaled by 0.3 and the bulk density was scaled by 0.7 to account for the combination of powder and solid material encountered by the melt pool on the downskin of a 45 deg surface.

Figure 13 compares the downskin roughness measurements scaled with predicted non-dimensional melt pool depth to scaling with volume energy density. The results show that the melt pool depth does a better job scaling the roughness compared to the volumetric energy density. For the same material and downskin surface angle, there is a decrease in roughness with depth, before increasing again. Note that the inflection point for the roughness trend occurs

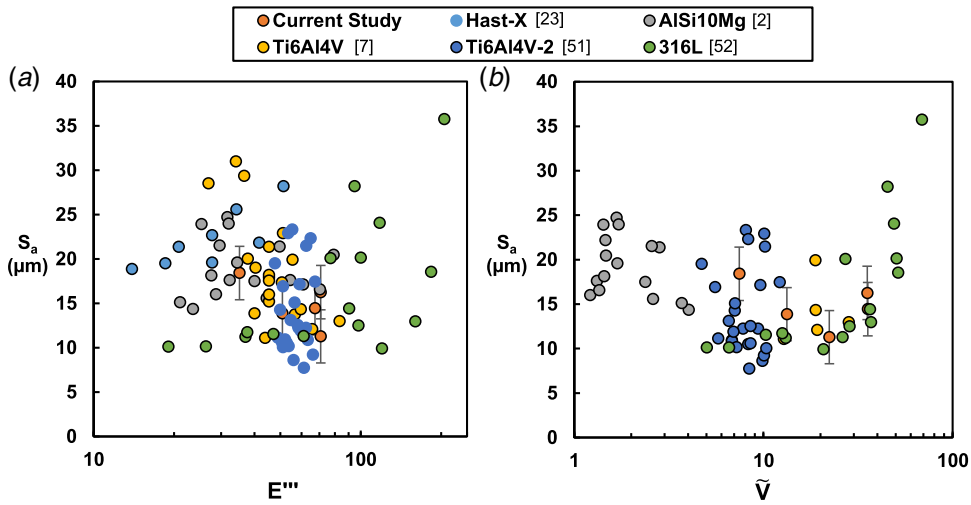

Fig. 12 Upskin roughness data from current study and studies from literature scaled with (*a*) volumetric energy density and (*b*) non-dimensional melt pool volume

Table 3 Material properties used for melt pool geometry predictions

	Hast-X	316L	AlSi10Mg	Ti6Al4V
Absorptivity	0.4	0.4	0.15	0.4
Laser spot radius (mm)	0.05	0.04	0.02	0.05, 0.1
Thermal conductivity (W/mK)	19	22	160	15
Density (kg/m^3)	8190	7900	2670	4500
Specific heat (J/kg K)	600	570	1200	1100
Liquidus temperature (K)	1473	1672	933	1900

at a non-dimensional depth of unity, where the melt pool depth matches the layer thickness. Tian et al. [23] also reported this result, where the minimum downskin roughness occurred when the depth of the melt pool was similar to the layer thickness. However, the 316L data do not scale well with the Hast-X data, using the non-dimensional depth parameter. More data are needed to understand how well this parameter accounts for roughness in different materials. It is likely that a more accurate estimate of the influence of the neighboring powder on material properties is needed to properly scale downskin roughness.

These results show promise to utilizing melt pool geometry to scale L-PBF roughness. However, given the sensitivity of the Rubenchik model to initial temperature and material properties, it is not recommended to develop a predictive correlation from this data at this time. Instead, the melt pool geometry scaling should be further investigated using more accurate properties based on *in situ* measurements or process simulations. For now, melt pool geometry predictions can serve as a helpful tool to understand roughness trends.

Contour Effects. Since contour laser passes are commonly used to control surface roughness in L-PBF, the effects of the contour process parameters on surface roughness were also explored. First, the effect of linear energy density, E', on surface roughness was considered on both the upskin and downskin. Given the contours are single laser passes, the linear energy density is a reasonable scaling to use. Three E' cases for each surface are presented in Fig. 14. For the upskin surface, the roughness decreased slightly

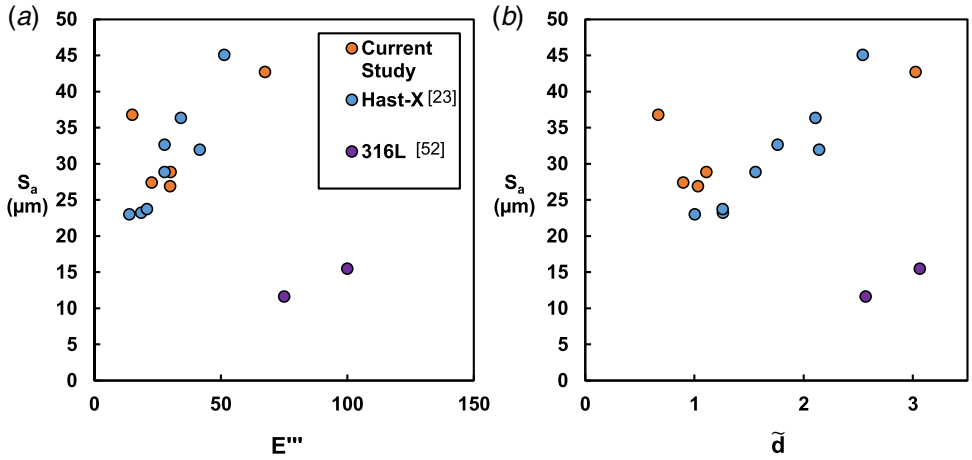

Fig. 13 Downskin roughness scaling based on (*a*) volumetric energy density and (*b*) non-dimensional melt pool depth

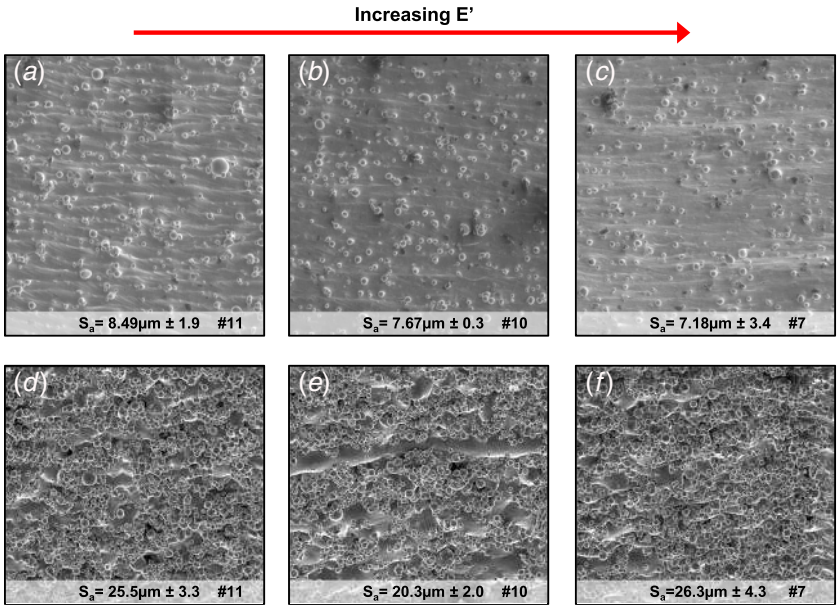

Fig. 14 SEM images of (*a*)–(c) upskin and (*d*)–(*f*) downskin surfaces showing the effect of contour energy input. E' is (*a*) 0.13 J/m, (*b*) 0.26 J/m, (c) 0.33 J/m, (*d*) 0.03 J/m, (e) 0.06 J/m, and (*f*) 0.1 J/m. Width of images is 1.4 mm.

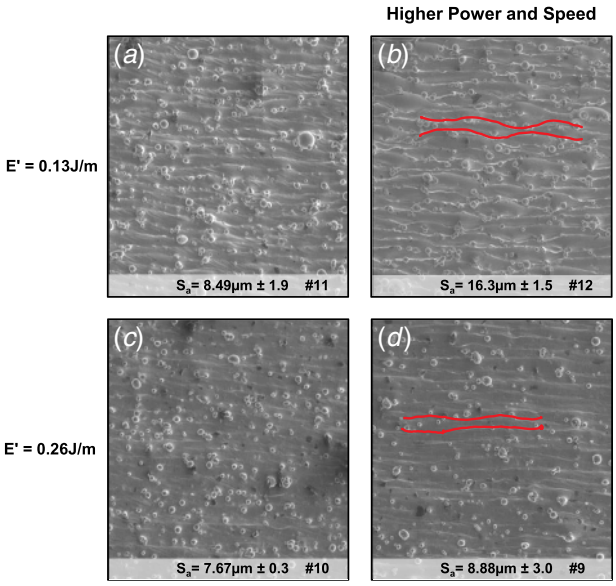

Fig. 15 SEM images of upskin surfaces with contour E' matched at two levels: (*a*) and (*b*) 0.13 J/m and (c) and (*d*) 0.26 J/m, but different laser powers and speeds. Red outlines highlight approximate edges of melt pools. Width of images is 1.4 mm. (Color version online.)

with increasing E'. However, the SEM images and the confidence intervals show that changes to roughness magnitude and morphology were not substantial.

On the other hand, the downskin roughness initially decreased with E' before increasing again for values greater than $E' = 0.06$ J/m. The lowest E' case shows evidence of the hatching roughness underneath the partially melted particles, while these roughness features appear to be partially eliminated in the medium E' case. In the high E' case, the level of partially melted particles was increased, as well as the presence of larger irregular roughness features. One hypothesis for these trends is that the low E' case did not penetrate far enough to melt the initial roughness features, the medium E' was an optimum amount of energy input, while the high E' case was too much energy input, with the contour penetrating deeper than intended. This trend is the same as with the downskin hatching in Fig. 13, where the lowest downskin roughness occurs when the penetration of the melt pool is close to the layer thickness.

While the roughness trends with E' are generally intuitive, the question remains whether E' correctly captures the physics for the contour passes. To investigate, the same test was carried out as was done with the hatching cases, where E' was matched with different laser powers and scan speeds. Images comparing two different matched E' levels for the upskin are shown in Fig. 15. For the low matched E', the higher laser power and scanning speed case resulted in a 1.7× increase in roughness magnitude and different surface morphology than the low power and speed case. The nonuniform weld cross section visible in Fig. 15(*b*) shows signs of Plateau-Rayleigh instabilities, indicating the melt pool was likely elongated. Interestingly, the difference in roughness magnitude was only 1.2× between the high E' matched cases. Figure 15(*d*) shows signs of hydrodynamic instabilities like Fig. 15(*b*) but to a lesser extent.

To understand these trends, the Rubenchik model [50] was again used to predict the melt pool dimensions based on non-dimensional parameters. The results of this analysis are shown in Table 4. The predictions show that samples 12 and 9 did indeed have long and thin melt pools relative to samples 11 and 10, confirming that the increase in roughness can be attributed to instabilities. Interestingly, the low E' cases had smaller melt pool depths than the high E' cases, which may explain the decreased presence of roughness due to instabilities. With a larger melt pool depth in the high E' case, less molten material was near the surface, reducing the available surface energy to drive Rayleigh instabilities. Therefore, to limit the roughness caused by instabilities with high aspect ratio melt pools, a higher E' should be used.

Similar comparisons were made for the downskin contours, shown in Fig. 16. The results show little difference in roughness when E' was matched while laser power and scan speed were increased. This result holds for both E' levels tested, with the lower E' level simply having a larger surface roughness magnitude. Given that this same insensitivity of the roughness to increased laser power and speed was seen with the downskin hatching, it is hypothesized that the same physical effect was at play for the contours. The depth of the melt pool was less sensitive to parameter changes that were made in this operating regime.

Since contours are used to improve the roughness of surfaces created by hatching, it was also of interest to determine how the pre-contour roughness level impacts the effectiveness of a given set of contour parameters. To generate this comparison, two different hatching parameters were used to establish different pre-contour roughness, shown for the upskin in Figs. 17(*a*) and 17(*c*). Then, the same contour was added to both of these surfaces to evaluate the change in roughness. The images in Figs. 17(*b*) and 17(*d*) show that the contour reduced the roughness of the upskin surface by remelting the roughness caused by the ends of the hatching vectors. Despite the different pre-contour roughness magnitudes, the post-contour roughness magnitude was similar for both cases. The result was a 36% and 57% reduction in roughness for the low and high pre-contours cases, respectively.

The same comparisons were made for the downskin surfaces, shown in Fig. 18. Interestingly, there was little change in the roughness magnitude for the low pre-contour roughness case. However, in the high pre-contour case, the same contour parameters resulted in a 56% decrease in roughness magnitude. This result is counter to what one might expect, where a given set of contour parameters would be less effective at reducing roughness when applied to larger pre-contour roughness magnitudes.

Given these results, it is hypothesized that the roughness preceding the contour affects the boundary conditions of the melt pool. Specifically, if the roughness of the pre-contour surface is larger, it will have a greater overlap with the contour scan pass, allowing the met pool to more directly contact the roughness. Thus, the energy of the contour is more concentrated on the roughness itself and less on the surrounding powder. To account for this effect, the beam offset (BO), or the shift of the laser position, could potentially be adjusted to better center the contour on the

Table 4 Melt pool size predictions for upskin contour parameters

	Melt pool predictions				Roughness		Contour parameters			
Sample #	w (μm)	d (μm)	l (μm)	l/w	S_a (μm)	±95% (μm)	P (W)	v (mm/s)	BO (mm)	E' (J/mm)
9	228	77	1047	4.6	8.88	3.0	214	840	0	0.26
10	219	79	556	2.5	7.67	0.3	107	420	0	0.26
11	169	51	448	2.6	8.49	1.9	88	700	0	0.13
12	173	50	824	4.8	16.3	1.5	176	1400	0	0.13

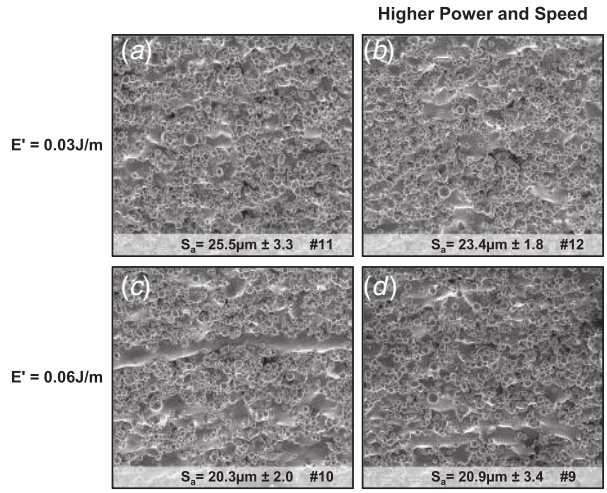

Fig. 16 SEM images of downskin surfaces with contour E' matched at two levels: (*a*) and (*b*) 0.03 J/m and (*c*) and (*d*) 0.06 J/m, but different laser powers and speeds. Width of images is 1.4 mm.

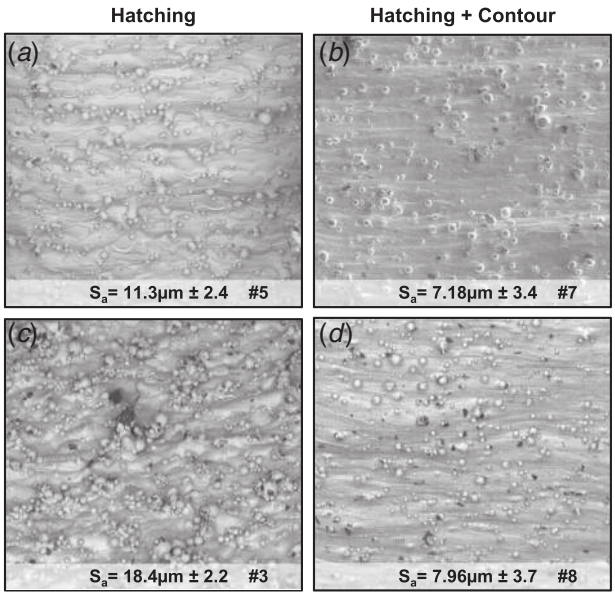

Fig. 17 SEM images of upskin surfaces showing roughness (*a*) and (c) before and (*b*) and (*d*) after contours with the same parameters at two different pre-contour roughness levels. Width of images is 1.4 mm.

roughness. The beam offset was not explored in this study. Nonetheless, the results herein highlight an important point: to maximize the effectiveness of downskin contours, the contour parameters must be properly tuned to the roughness of surface that precedes them.

Part Level Roughness Trends

One variable not explicitly evaluated in this study was the scanning strategy of the laser. Some studies have shown the impact of the scanning strategy on roughness [25,36], particularly the variation through the layers. Rotating the scan vectors by 67 deg each layer, as was done in the current study, has been shown to work well to minimize layerwise buildup of residual stresses and roughness. Nonetheless, patterns in the roughness data were evaluated in

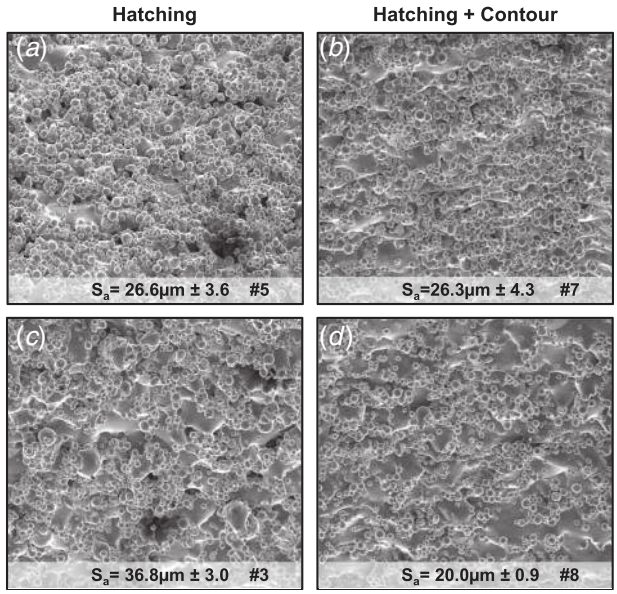

Fig. 18 SEM images of downskin surfaces showing roughness (*a*) and (c) before and (*b*) and (*d*) after contours with the same parameters at two different pre-contour roughness levels. Width of images is 1.4 mm.

this study to understand impact of process parameters on roughness related to the scanning strategy.

To determine the trends in roughness throughout the layers of the test elements, CT data were utilized since it resolved all surfaces of the test elements in full 3D. Instead of measuring the roughness heights individually, the cross-sectional area of the channels was used to represent changes to the large-scale roughness features on the channel walls simultaneously. An image processing technique was used to measure the area of each CT scan slice of the channel, building a dataset of channel area as a function of distance in the build direction. Autocorrelation was then used to search for trends in the layerwise area data for each channel. Before processing, large-scale trends in each dataset were removed with a second-order polynomial to increase the robustness of the autocorrelation operation.

While the resolution of the CT data was lower than the optical profilometry data, the CT data were still useful in evaluating large-scale roughness. In effect, using the CT data to analyze roughness is analogous to applying a low pass filter to the surface, removing the smaller roughness features such as partially melted particles. This filtering allows a clearer view of the trends tied to larger roughness features, such as dross.

Figure 19 shows the results from the autocorrelation for each channel from two different test elements. A perfect correlation of the data has a value of one, which is expected at a position of zero on the *x*-axis. For a random dataset, the autocorrelation is expected to quickly decay exponentially to zero and oscillate within the confidence band (grayed out region in Fig. 19). Alternatively, the autocorrelation of a periodic function is also periodic. Therefore, if there is a periodic pattern hidden in the layerwise area data, the autocorrelation should highlight this trend. Indeed, the autocorrelation for sample 1 in Fig. 19(*a*) shows a periodic trend, particularly for channels 1 and 3. Examining the spacing between the peaks gives an approximate frequency of eight layers for channels 1 and 16 layers for channel 3. The autocorrelation for sample 5 in Fig. 19(*b*), on the other hand, does not show a distinct periodic pattern with layers, although there is increased correlation around 52 layers.

To find a cause for the patterns identified, a generic analysis of the hatching vectors was performed. When considering the effect of hatching on roughness, the boundary conditions of the melt pool as it approaches or retreats from the edge of the part will

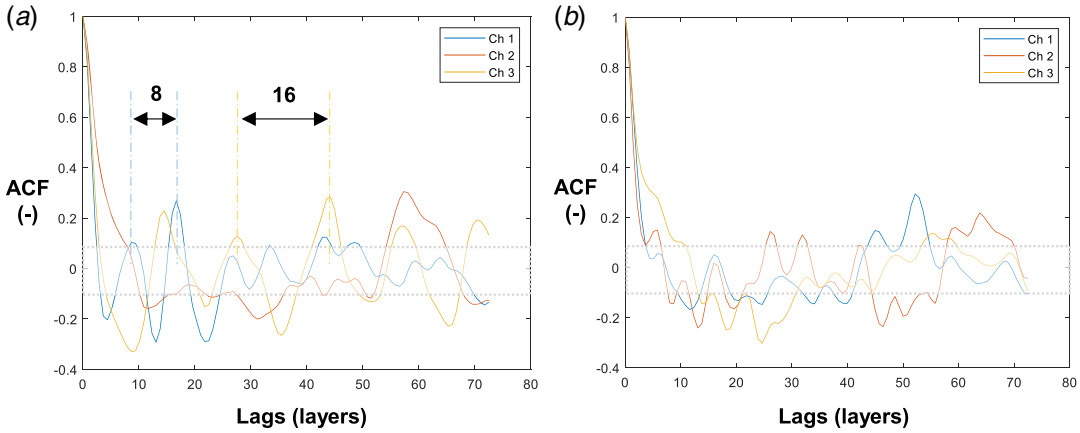

Fig. 19 Autocorrelation of the CT channel area for (*a*) sample 1 and (*b*) sample 5. ACF, autocorrelation function.

determine the shape of the melt pool, and subsequently the surface of the part. Therefore, the angle of the laser scan vector relative to the edge of a part is more relevant than the angle of vector rotation between layers. Figure 20(*a*) illustrates the angle θ between the scan vectors and the normal of the edge of the part. Given the test element geometry shown in Fig. 6, vectors with the same positive and negative values of θ would result in the same boundary conditions for the majority of the channel walls. Therefore, the absolute value of θ was taken over 300 layers using an inter-layer vector rotation of 67 deg. The results, shown in Fig. 20(*b*), indicate

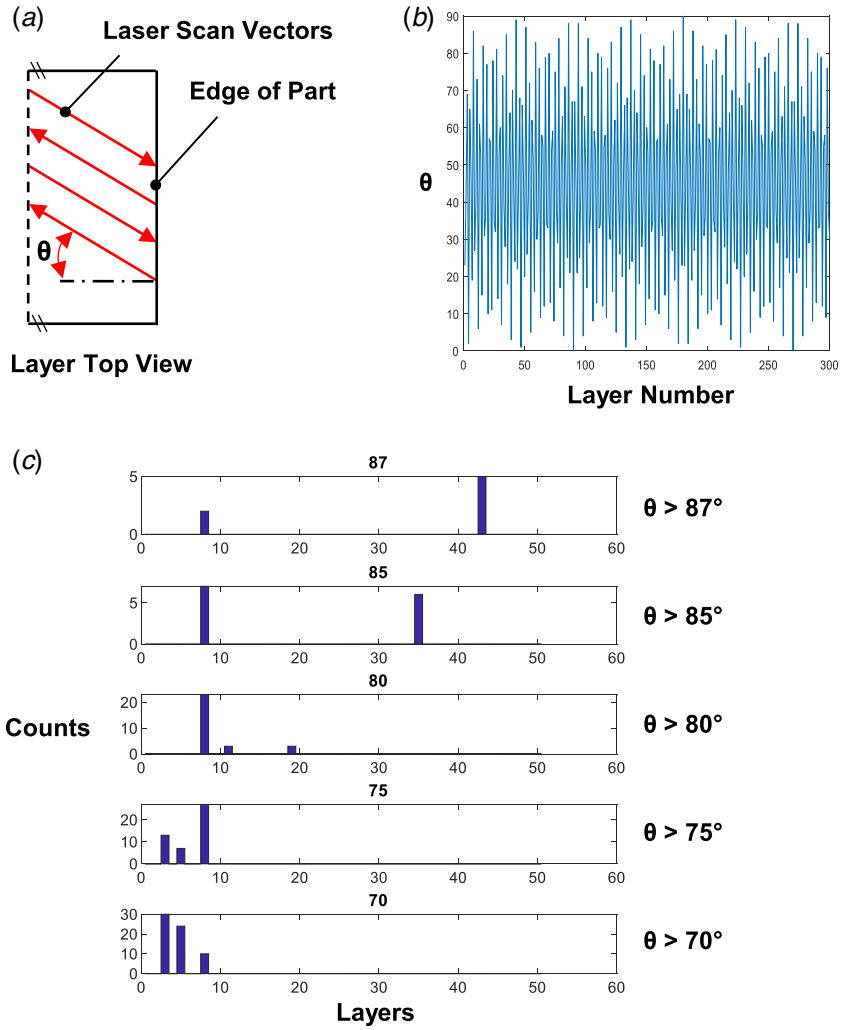

Fig. 20 (*a*) Angle of scan vectors relative to the edge normal for an arbitrary section of part. (*b*) Variation of θ with layer number using 67 deg rotation of scan vectors between layers. (*c*) Histograms showing dominant peak spacing frequencies from Fig. 20(*b*) for peaks greater than 70, 75, 80, 85, and 87 deg.

that a repeating pattern exists in θ as the build progresses through the layers.

The spacing between peaks in Fig. 20(*b*) was calculated based on different minimum angles, shown in the histograms of Fig. 20(*c*). The histogram count represents number of peaks with the same layerwise period. The largest effect on roughness is assumed to be from extreme angles—the difference in melt pool boundary conditions is most significant between 90 deg and 0 deg, for example. Therefore, only angles greater than 70 deg were considered. For all angles considered in Figs. 20(*c*) and 20(*a*), common frequency was eight layers. Additional frequencies of 43 and 35 layers were seen for angles greater than 87 deg and 85 deg, respectively.

Looking back to the periods identified from the area autocorrelation data in Fig. 19, there appears to be a correlation to the hatching patterns. For example, the periods in the data from sample 1 were 1× and 2× eight-layer hatching pattern period seen in Fig. 20(*c*). On the other hand, the patterns in the sample 5 data only correlate with the higher frequency hatching patterns around 35 layers. Given the earlier melt pool analysis predicted sample 1 having a larger melt pool volume than sample 5, it is hypothesized that larger melt pools illuminate recurring patterns in the scanning strategy. With the smaller melt pools in sample 5, only the most extreme, low frequency scanning patterns are manifested in the large-scale roughness features.

While this scan vector analysis did not take into account the actual positions of the scan vectors, the analysis illustrates the connections between large-scale roughness features and the hatching pattern. Consequently, to truly control L-PBF surface roughness, understanding and controlling the scanning strategy is required.

Conclusions

Overall, AM surface roughness is a complex issue that is well known, but ill characterized. Many have measured roughness in different applications, but few have succeeded in determining causal relationships due to the large number of variables at play. The current study has explored the influence of certain process parameters on the roughness of AM surfaces. Through these comparisons, certain local and global roughness trends have been identified and discussed.

To start, the ineffectiveness of thermodynamic scalings, such as volume energy density, at describing surface roughness trends has been shown. Matching the volumetric energy density does not result in the same roughness, even when the part, surface, machine, and material are matched. Alternatively, predictions of melt pool geometry using physics-based correlations were shown to be better suited to explaining roughness trends. For example, a melt pool-based scaling identified the minimum downskin roughness occurring when the melt pool depth was equal to the layer thickness.

Analysis of roughness trends has also shown that the upskin and downskin roughness is sensitive to different parameters. For the upskin, the roughness is tied to the overall size of the melt pool, which is a function of many parameters and properties. Preliminary scalings show that the total melt pool volume may be a good predictor of surface roughness. On the other hand, downskin surfaces are most sensitive to the melt pool depth, which can be reliably scaled with laser power and scanning speed alone. However, more data are needed to develop a comprehensive understanding of the relationship between surface roughness and melt pool geometry before accurate scalings can be developed.

Contours have been shown to generally reduce surface roughness when tuned properly. However, for the upskin surface, the size of the melt pool must be limited to avoid increases in roughness due to hydrodynamic instabilities. These instabilities can be mitigated if higher linear energy densities are used. The downskin surface is less sensitive to changes in laser power and speed, with the roughness being tied mainly to the depth of the melt pool. However, the roughness of the surface preceding a downskin contour has a large influence on the final surface roughness. Therefore, downskin contour parameters must be tuned considering the surface that precedes them.

The hatching strategy was also shown to cause patterns in large-scale roughness features throughout the part. In cases where the process parameters resulted in large melt pools, repeating directions of the hatch vectors were shown to correlate with patterns in the large features of the internal channels. Thus, scanning strategies must be understood and controlled to successfully regulate surface roughness.

Overall, this work has provided insight into some of the roughness phenomena seen with laser powder bed fusion. Although preliminary, scaling based on the melt pool geometry shows promise for predicting surface roughness trends. This result, coupled with the findings of layerwise roughness patterns, points to a need to develop local roughness predictions based on part geometry, scanning strategy, laser parameters, and material properties. Ultimately, this work has laid the foundation for understanding and controlling surface roughness in the L-PBF process, which is paramount in developing AM parts for a wide variety of applications.

Funding Data

- The authors would like to thank the U.S. Department of Energy National Energy Technology Laboratory for sponsoring research presented in this paper. This paper is based upon work supported by the Department of Energy under Award Number DE-FE0025011.

Conflict of Interest

This report was prepared as an account of work sponsored by an agency of the United States Government. Neither the United States Government nor any agency thereof, nor any of their employees, makes any warranty, express or implied, or assumes any legal liability or responsibility for the accuracy, completeness, or usefulness of any information, apparatus, product, or process disclosed, or represents that its use would not infringe privately owned rights. Reference herein to any specific commercial product, process, or service by trade name, trademark, manufacturer, or otherwise does not necessarily constitute or imply its endorsement, recommendation, or favoring by the United States Government or any agency thereof. The views and opinions of authors expressed herein do not necessarily state or reflect those of the United States Government or any agency thereof.

Nomenclature

a = laser spot diameter
d = melt pool depth
k = thermal conductivity
p = ratio of melt pool time scales
t = layer thickness
v = laser scanning speed
w = melt pool width
z = depth or surface normal dimension
A = laser absorptivity
C = specific heat capacity
L = channel length, hole length, and melt pool length
P = laser power
R = specific gas constant
V = volume
A_c = cross-sectional area
A_s = surface area
H_d = laser hatch distance
R_a = arithmetic mean surface roughness
T_m = melting temperature

E' = linear energy density
E'' = surface energy density
E''' = volume energy density

Greek Symbols

α = thermal diffusivity
β = ratio of enthalpy input to enthalpy of melting

References

[1] Badrossamay, M., Yasa, E., Van Vaerenbergh, J., and Kruth, J.-P., 2009, "Improving Productivity Rate in SLM of Commercial Steel Powders," Rapid 2009 Conference and Expo, Schaumburg, IL, pp. 1–9.
[2] Calignano, F., Manfredi, D., Ambrosio, E. P., Iuliano, L., and Fino, P., 2013, "Influence of Process Parameters on Surface Roughness of Aluminum Parts Produced by DMLS," Int. J. Adv. Manuf. Technol., **67**(9–12), pp. 2743–2751.
[3] Hamidi, M., Gastaldi, D., Francesca, N., and Vedani, M., 2018, "On Morphological Surface Features of the Parts Printed by Selective Laser Melting (SLM)," Addit. Manuf., **24**(October), pp. 373–377.
[4] Pupo, Y., Monroy, K. P., and Ciurana, J., 2015, "Influence of Process Parameters on Surface Quality of CoCrMo Produced by Selective Laser Melting," Int. J. Adv. Manuf. Technol., **80**(5–8), pp. 985–995.
[5] Qiu, C., Panwisawas, C., Ward, M., Basoalto, H. C., Brooks, J. W., and Attallah, M. M., 2015, "Acta Materialia on the Role of Melt Flow Into the Surface Structure and Porosity Development During Selective Laser Melting," Acta Mater., **96**, pp. 72–79.
[6] Shrestha, S., and Chou, K., 2017, "A Build Surface Study of Powder-Bed Electron Beam Additive Manufacturing by 3D Thermo-Fluid Simulation and White-Light Interferometry," Int. J. Mach. Tools Manuf., **121**(April), pp. 1–13.
[7] Simchi, A., 2004, "The Role of Particle Size on the Laser Sintering of Iron Powder," Metall. Mater. Trans. B, **35**(5), pp. 937–948.
[8] Spierings, A. B. B., Herres, N., Levy, G., and Authors, F., 2011, "Influence of the Particle Size Distribution on Surface Quality and Mechanical Properties in AM Steel Parts," Rapid Prototyp. J., **17**(3), pp. 195–202.
[9] Wang, D., Liu, Y., Yang, Y., and Xiao, D., 2016, "Theoretical and Experimental Study on Surface Roughness of 316L Stainless Steel Metal Parts Obtained Through Selective Laser Melting," Rapid Prototyp. J., **22**(4), pp. 706–716.
[10] Wang, D., Yang, Y., Yi, Z., and Su, X., 2013, "Research on the Fabricating Quality Optimization of the Overhanging Surface in SLM Process," Int. J. Adv. Manuf. Technol., **65**(9–12), pp. 1471–1484.
[11] Wang, L. Z., Wang, S., and Wu, J. J., 2017, "Experimental Investigation on Densification Behavior and Surface Roughness of AlSi10Mg Powders Produced by Selective Laser Melting," Opt. Laser Technol., **96**, pp. 88–96.
[12] Yadroitsev, I., and Smurov, I., 2011, "Surface Morphology in Selective Laser Melting of Metal Powders," Phys. Procedia, **12**, pp. 264–270.
[13] Casalino, G., Campanelli, S. L., Contuzzi, N., and Ludovico, A. D., 2015, "Experimental Investigation and Statistical Optimisation of the Selective Laser Melting Process of a Maraging Steel," Opt. Laser Technol., **65**, pp. 151–158.
[14] Yakout, M., Cadamuro, A., Elbestawi, M. A., and Veldhuis, S. C., 2017, "The Selection of Process Parameters in Additive Manufacturing for Aerospace Alloys," Int. J. Adv. Manuf. Tech., **92**, pp. 2081–2098.
[15] Cherry, J. A., Davies, H. M., Mehmood, S., Lavery, N. P., Brown, S. G. R., and Sienz, J., 2014, "Investigation Into the Effect of Process Parameters on Microstructural and Physical Properties of 316L Stainless Steel Parts by Selective Laser Melting," Int. J. Adv. Manuf. Technol., **76**(5–8), pp. 869–879.
[16] DePond, P. J., Guss, G., Ly, S., Calta, N. P., Deane, D., Khairallah, S., and Matthews, M. J., 2018, "In Situ Measurements of Layer Roughness During Laser Powder Bed Fusion Additive Manufacturing Using Low Coherence Scanning Interferometry," Mater. Des., **154**, pp. 347–359.
[17] Kruth, J., Badrossamay, M., Yasa, E., Deckers, J., Thijs, L., and Van Humbeeck, J., 2010, "Part and Material Properties in Selective Laser Melting of Metals," Proceedings of the 16th International Symposium on Electromachining, Shanghai, China, Apr. 19–23.
[18] Li, Z., Kucukkoc, I., Zhang, D. Z., and Liu, F., 2018, "Optimising the Process Parameters of Selective Laser Melting for the Fabrication of Ti6Al4V Alloy," Rapid Prototyp. J., **24**(1), pp. 150–159.
[19] Liu, B., Wildman, R., Tuck, C., Ashcroft, I., and Hague, R., 2011, "Investigation the Effect of Particle Size Distribution on Processing Parameters Optimisation in Selective Laser Melting Process," Proceedings of the Annual International Solid Freeform Fabrication Symposium, Austin, TX, pp. 227–238, University of Texas at Austin.
[20] Mohammadi, M., and Asgari, H., 2018, "Achieving Low Surface Roughness AlSi10Mg 200C Parts Using Direct Metal Laser Sintering," Addit. Manuf., **20**, pp. 23–32.
[21] Mumtaz, K., and Hopkinson, N., 2009, "Top Surface and Side Roughness of Inconel 625 Parts Processed Using Selective Laser Melting," Rapid Prototyp. J., **15**(2), pp. 96–103.
[22] Yang, T., Liu, T., Liao, W., Macdonald, E., Wei, H., and Chen, X., 2019, "The Influence of Process Parameters on Vertical Surface Roughness of the AlSi10Mg Parts Fabricated by Selective Laser Melting," J. Mater. Process. Technol., **266**(September 2018), pp. 26–36.
[23] Tian, Y., Tomus, D., Rometsch, P., and Wu, X., 2016, "Influences of Processing Parameters on Surface Roughness of Hastelloy X Produced by Selective Laser Melting," Addit. Manuf., **13**, pp. 103–112.
[24] Cabanettes, F., Joubert, A., Chardon, G., Dumas, V., Rech, J., Grosjean, C., and Dimkovski, Z., 2018, "Topography of as Built Surfaces Generated in Metal Additive Manufacturing: A Multi Scale Analysis From Form to Roughness," Precis. Eng., **52**(October 2017), pp. 249–265.
[25] Cloots, M., Spierings, A. B., and Wegener, K., 2013, "Assessing New Support Minimizing Strategies for the Additive Manufacturing Technology SLM," Solid Freeform Fabrication Symposium, Austin, TX, August 12.
[26] Fox, J. C., Moylan, S. P., and Lane, B. M., 2016, "Effect of Process Parameters on the Surface Roughness of Overhanging Structures in Laser Powder Bed Fusion Additive Manufacturing," Procedia CIRP, **45**, pp. 131–134.
[27] Covarrubias, E. E., and Eshraghi, M., 2018, "Effect of Build Angle on Surface Properties of Nickel Superalloys Processed by Selective Laser Melting," JOM, **70**(3), pp. 336–342.
[28] Kleszczynski, S, Ladewig, A, Friedberger, K, Zur Jacobsmühlen, J, Merhof, D, and Witt, G, 2015, "Position Dependency of Surface Roughness in Parts From Laser Beam," 26th International Solid Free Form Fabrication (SFF) Symposium, Austin, TX, August 10.
[29] Koutiri, I., Pessard, E., Peyre, P., Amlou, O., and De Terris, T., 2018, "Influence of SLM Process Parameters on the Surface Finish, Porosity Rate and Fatigue Behavior of As-Built Inconel 625 Parts," J. Mater. Process. Technol., **255**(June 2017), pp. 536–546.
[30] Yasa, E., and Kruth, J. P., 2011, "Application of Laser Re-Melting on Selective Laser Melting Parts," Adv. Prod. Eng. Manage., **6**, pp. 259–270.
[31] Yasa, E., Kruth, J., and Deckers, J., 2011, "Manufacturing Technology Manufacturing by Combining Selective Laser Melting and Selective Laser Erosion/Laser Re-Melting," CIRP Ann., **60**(1), pp. 263–266.
[32] Yasa, E., and Kruth, J., 2010, "Investigation of Laser and Process Parameters for Selective Laser Erosion," **34**, pp. 101–112.
[33] Alrbaey, K., Wimpenny, D., Tosi, R., Manning, W., and Moroz, A., 2014, "On Optimization of Surface Roughness of Selective Laser Melted Stainless Steel Parts: A Statistical Study," J. Mater. Eng. Perform., **23**(6), pp. 2139–2148.
[34] Vaithilingam, J., Goodridge, R. D., Hague, R. J. M., Christie, S. D. R., and Edmondson, S., 2016, "Journal of Materials Processing Technology the Effect of Laser Remelting on the Surface Chemistry of Ti6al4V Components Fabricated by Selective Laser Melting," J. Mater. Process. Technol., **232**, pp. 1–8.
[35] Ahn, I. H., Moon, S. K., Bi, G., and Wei, J., 2016, "Influence of the Geometric Factor for the Width of the Contour Scan in Selective Laser Melting," Proceedings of the 2nd International Conference on Progress in Additive Manufacturing, Singapore.
[36] Sarkar, S., Porwal, A., Yaswanth, N., and Nath, A. K., 2018, "A Study on Effect of Different Process Parameters on the Quality of Overhang Surface Produced by Selective Laser Melting," ASME 2018 13th International Manufacturing Science and Engineering Conference, College Station, TX, June 18–22, pp. 1–7.
[37] Kudzal, A., Mcwilliams, B., Hofmeister, C., Kellogg, F., Yu, J., Taggart-scarff, J., and Liang, J., 2017, "Effect of Scan Pattern on the Microstructure and Mechanical Properties of Powder Bed Fusion Additive Manufactured 17-4 Stainless Steel," Mater. Des., **133**, pp. 205–215.
[38] Liu, B., Wildman, R., Tuck, C., Ashcroft, I., and Hague, R., 2011, "Investigation the Effect of Particle Size Distribution on Processing Parameters Optimization in Selective Laser Melting Process," SFF, Austin, TX.
[39] Del Re, F., Contaldi, V., Astarita, A., Palumbo, B., Squillace, A., Corrado, P., and Di Petta, P., 2018, "Statistical Approach for Assessing the Effect of Powder Reuse on the Final Quality of AlSi10Mg Parts Produced by Laser Powder Bed Fusion Additive Manufacturing," Int. J. Adv. Manuf. Technol., **97**(5–8), pp. 2231–2240.
[40] Jamshidinia, M., and Kovacevic, R., 2015, "The Influence of Heat Accumulation on the Surface Roughness in Powder-Bed Additive Manufacturing," Surf. Topogr. Metrol. Prop., **3**(1), p. 014003.
[41] Stimpson, C. K., Snyder, J. C., Thole, K. A., and Mongillo, D., 2016, "Scaling Roughness Effects on Pressure Loss and Heat Transfer of Additively Manufactured Channels," ASME J. Turbomach., **139**(2), p. 021003.
[42] Matthews, M. J., Guss, G., Khairallah, S. A., Rubenchik, A. M., Depond, P. J., and King, W. E., 2016, "Acta Materialia Denudation of Metal Powder Layers in Laser Powder Bed Fusion Processes," Acta Mater., **114**, pp. 33–42.
[43] Bidare, P., Bitharas, I., Ward, R. M., Attallah, M. M., and Moore, A. J., 2018, "Fluid and Particle Dynamics in Laser Powder Bed Fusion," Acta Mater., **142**, pp. 107–120.
[44] Mukherjee, T., Manvatkar, V., De, A., and Debroy, T., 2017, "Dimensionless Numbers in Additive Manufacturing," J. Appl. Phys., **121**-(064904), p. 64904.
[45] Wang, L., Wei, Q. S., Shi, Y. S., Liu, J. H., and He, W. T., 2011, "Experimental Investigation Into the Single-Track of Selective Laser Melting of IN625," Adv. Mater. Res., **233–235**, pp. 2844–2848.
[46] Yadroitsev, I., Yadroitsava, I., Bertrand, P., and Smurov, I., 2012, "Factor Analysis of Selective Laser Melting Process Parameters and Geometrical Characteristics of Synthesized Single Tracks," Rapid Prototyp. J., **18**(3), pp. 201–208.
[47] Bertoli, U. S., Wolfer, A. J., Matthews, M. J., Delplanque, J. R., and Schoenung, J. M., 2017, "On the Limitations of Volumetric Energy Density as a Design Parameter for Selective Laser Melting," JMADE, **113**, pp. 331–340.

[48] King, W. E., Barth, H. D., Castillo, V. M., Gallegos, G. F., Gibbs, J. W., Hahn, D. E., Kamath, C., and Rubenchik, A. M., 2014, "Journal of Materials Processing Technology Observation of Keyhole-Mode Laser Melting in Laser Powder-Bed Fusion Additive Manufacturing," J. Mater. Process. Technol., **214**(12), pp. 2915–2925.
[49] Hann, D. B., Iammi, J., and Folkes, J., 2011, "A Simple Methodology for Predicting Laser-Weld Properties From Material and Laser Parameters," J. Phys. D Appl. Phys., **44**(44).
[50] Rubenchik, A. M., King, W. E., and Wu, S. S., 2018, "Scaling Laws for the Additive Manufacturing," J. Mater. Process. Technol., **257**(October 2017), pp. 234–243.
[51] Khorasani, A. M., Gibson, I., and Ghaderi, A. R., 2018, "Rheological Characterization of Process Parameters Influence on Surface Quality of Ti-6Al-4V Parts Manufactured by Selective Laser Melting," Int. J. Adv. Manuf. Technol., **V**(9–12), pp. 3761–3775.
[52] Aqilah, D. N., Sayuti, A. K. M., Farazila, Y., Suleiman, D. Y., Amirah, M. A. N., and Izzati, W. B. W. N., 2018, "Effects of Process Parameters on the Surface Roughness of Stainless Steel 316L Parts Produced by Selective Laser Melting," J. Test. Eval., **46**(4), p. 20170140.
[53] Boschetto, A., Bottini, L., and Veniali, F., 2017, "Roughness Modeling of AlSi10Mg Parts Fabricated by Selective Laser Melting," J. Mater. Process. Technol., **241**, pp. 154–163.
[54] Leary, M., 2016, *Surface Roughness Optimisation for Selective Laser Melting (SLM): Accommodating Relevant and Irrelevant Surfaces*, Elsevier Ltd., New York.
[55] Stimpson, C. K., Snyder, J. C., Thole, K. A., and Mongillo, D., 2017, "Scaling Roughness Effects on Pressure Loss and Heat Transfer of Additively Manufactured Channels," ASME J. Turbomach., **139**(2).
[56] Grimm, T., Wiora, G., and Witt, G., 2015, "Characterization of Typical Surface Effects in Additive Manufacturing With Confocal Microscopy," Surf. Topogr. Metrol. Prop., **3**(1), p. 014001.
[57] Wang, D., Mai, S., Xiao, D., and Yang, Y., 2016, "Surface Quality of the Curved Overhanging Structure Manufactured From 316-L Stainless Steel by SLM," Int. J. Adv. Manuf. Technol., **86**(1–4), pp. 781–792.